Broad-band spatial light modulation with dual epsilon-near-zero modes

Long Wen[1†], Xianghong Nan[1†], Jiaxiang Li[1], David R. S. Cumming[3*], Xin Hu[2*] and Qin Chen [1*]

Epsilon-near-zero (ENZ) modes have attracted extensive interests due to its ultrasmall mode volume resulting in extremely strong light-matter interaction (LMI) for active optoelectronic devices. The ENZ modes can be electrically toggled between on and off states with a classic metal-insulator-semiconductor (MIS) configuration and therefore allow access to electro-absorption (E-A) modulation. Relying on the quantum confinement of charge-carriers in the doped semiconductor, the fundamental limitation of achieving high modulation efficiency with MIS junction is that only a nanometer-thin ENZ confinement layer can contribute to the strength of E-A. Further, for the ENZ based spatial light modulation, the requirement of resonant coupling inevitably leads to small absolute modulation depth and limited spectral bandwidth as restricted by the properties of the plasmonic or high-Q resonance systems. In this paper, we proposed and demonstrated a dual-ENZ mode scheme for spatial light modulation with a TCOs/dielectric/silicon nanotrench configuration for the first time. Such a SIS junction can build up two distinct ENZ layers arising from the induced charge-carriers of opposite polarities adjacent to both faces of the dielectric layer. The non-resonant and low-loss deep nanotrench framework allows the free space light to be modulated efficiently *via* interaction of dual ENZ modes in an elongated manner. Our theoretical and experimental studies reveal that the dual ENZ mode scheme in the SIS configuration leverages the large modulation depth, extended spectral bandwidth together with high speed switching, thus holding great promise for achieving electrically addressed spatial light modulation in near- to mid-infrared regions.

Keywords: epsilon-near-zero; modulation; TCOs; electro-optic; light harvesting

Introduction

Active controlling the characteristics of the optical signal in amplitude, phase or polarization is essential for a broad application in diverse fields such as optical processing, optical interconnects, adaptive optics, image projection, optical sensing etc.[1–7]. Tremendous efforts have been made in the past decades towards realizing electrically addressed modulation by carrier dispersion, the Pockels, or quantum confined Stark effect[8–10]. To meet the ever-increasing demands for modern photonic systems, advanced modulation solutions should encompass not only the high speed and efficient operation, but also the low energy consumption and capability of large-scale integration. Therefore, electro-optic (E-O) modulation on the all-silicon or silicon compatible platform has

[1]Institute of Nanophotonics, Jinan University, Guangzhou 511443, China; [2]Hangzhou Dianzi University, Hangzhou 310018, China; [3]James Watt School of Engineering, University of Glasgow, Glasgow G12 8QQ, UK.

[†]These authors contributed equally to this work.

*Correspondence: RSC David, E-mail: david.cumming.2@glasgow.ac.uk; X Hu, E-mail: xin.hu@hdu.edu.cn;
Q Chen, E-mail: chenqin2018@jnu.edu.cn

continued to be at the forefront of research in this field[11−13]. The inherent weak E-O effect of silicon is the major stumbling block to achieve efficient all-silicon modulation. By employing a high-Q (quality factor) resonant configuration, the silicon modulation in the integrated optics domains has been struggled to satisfy large modulation depth and desired high speed simultaneously, however at the expense of limited spectral bandwidth[14−17]. In contrast, it becomes even more challenging to realize spatial light modulation relying on silicon E-O effect. Nevertheless, several light-matter interaction (LMI) enhancing strategies have been proposed to achieve silicon-based spatial light modulation[17−24]. For example, the free carrier electro-refraction (E-R) effect of silicon can be greatly enhanced by incorporating plasmonic design into a metal-oxide-seminconductor (MOS) capacitor configuration[18−20]. However, as the resonant plasmonic structures are always accompanied by serious Ohmic loss, it is hardly possible to achieve large absolute modulation depth. Alternately, the photonic-crystal (PhC) cavity has been implemented in silicon spatial light modulators, where the enhanced E-R serves as a perturbation to the critical coupled high-Q resonance[21−24]. Despite the improved modulation depth, such a sensitive high-Q system suffers from narrow spectral bandwidth (typically less than 1 nm in the PhC structure[21,22]) and intrinsic poor angular tolerance. The silicon compatible platform with hybrid integration of active medium facilitates the utilization of more efficient E-O mechanisms for free space light modulation[1,2,25−28]. For instance, the liquid crystal on silicon (LCoS) is the most mature technology for spatial light manipulation and has been widely used on both the basic researches and practical applications[25]. Because of the E-O response of the nematic liquid crystal is typically in the millisecond scale, the main limitation of LCoS technique lies on its slow switching speed. Fabry-Perot cavity with embedded multiple quantum well layers (Ge/SiGe or Ⅲ-Ⅴ MQW) have also been used to create spatial light modulators on silicon[26−29]. The operation spectral bandwidth is also narrow as the band-edge absorption of MQW occurs at a precisely selected wavelength. Moreover, the hybrid integration of MQW/Si requires sophisticated, complex and expensive fabrication techniques such as multilayer heteroepitaxy or wafer-bonding.

Recently, the epsilon-near-zero (ENZ) effect based on the transparent conducting oxides (TCOs) has emerged as a robust LMI enhancing scheme for all-optical switch,

E-O modulation, perfect absorption/thermal emission-and, etc[30−33]. In particular, the onset and offset of ENZ confinement on nanometer thick carrier accumulation/depletion layer can be dynamically controlled via classic MOS configuration on the silicon platform. This makes the TCO as a compelling choice for hybrid integration on silicon to achieve more efficient E-O modulation for both the waveguide integrated and free-space optics[36−43]. In most previous literatures, metal or metal-like materials (e.g. ionic liquids) were used as the gate electrodes while TCO served as the ground semiconductor[33−36]. The E-O response was achieved upon tuning the carrier density of TCO to match or mismatch the ENZ condition. In other scenarios where silicon is used as the gate electrode[36−38,44,45], it is should be recalled that an electrostatic potential across the capacitor can also induce carrier accumulation, depletion and inversion in the gate semiconductor. However, those previous studies have normally considered TCO as the sole active medium but seldom explored the carrier dispersion effect in the silicon gate, which may hinder the possible contributions of the E-O or even ENZ responses from silicon. In this work, we demonstrate that broad spectral bandwidth modulation can be achieved in a TCOs/insulator/silicon nanotrench configuration due to the coexistence of ENZ confinements in both thesilicon and TCO. The nanotrench array with a high aspect ratio resembles a vertically aligned waveguide system with low optical loss in the absence of external voltage biasing across the junction. Dual ENZ modes form alongside the nanotrench sidewall when applying a voltage bias, because of the surface carrier accumulation at the both sides of the junction. These highly confined modes propagate in an elongated manner leading to very efficient electro-absorption. Compared to the plasmonic resonance strategy[40−43], the non-resonant and metal-less configuration allows for more efficient spatial light modulation with large absolute modulation depth and broadband spectral operation from near- to mid-infrared. Moreover, to the best of our knowledge, this study presents the first evidence of such a novel phenomenon that the ENZ-based electro-absorption effect can be achieved in silicon and applicable for spatial light modulation.

Dual ENZ-mode for broad-band E-O modulation

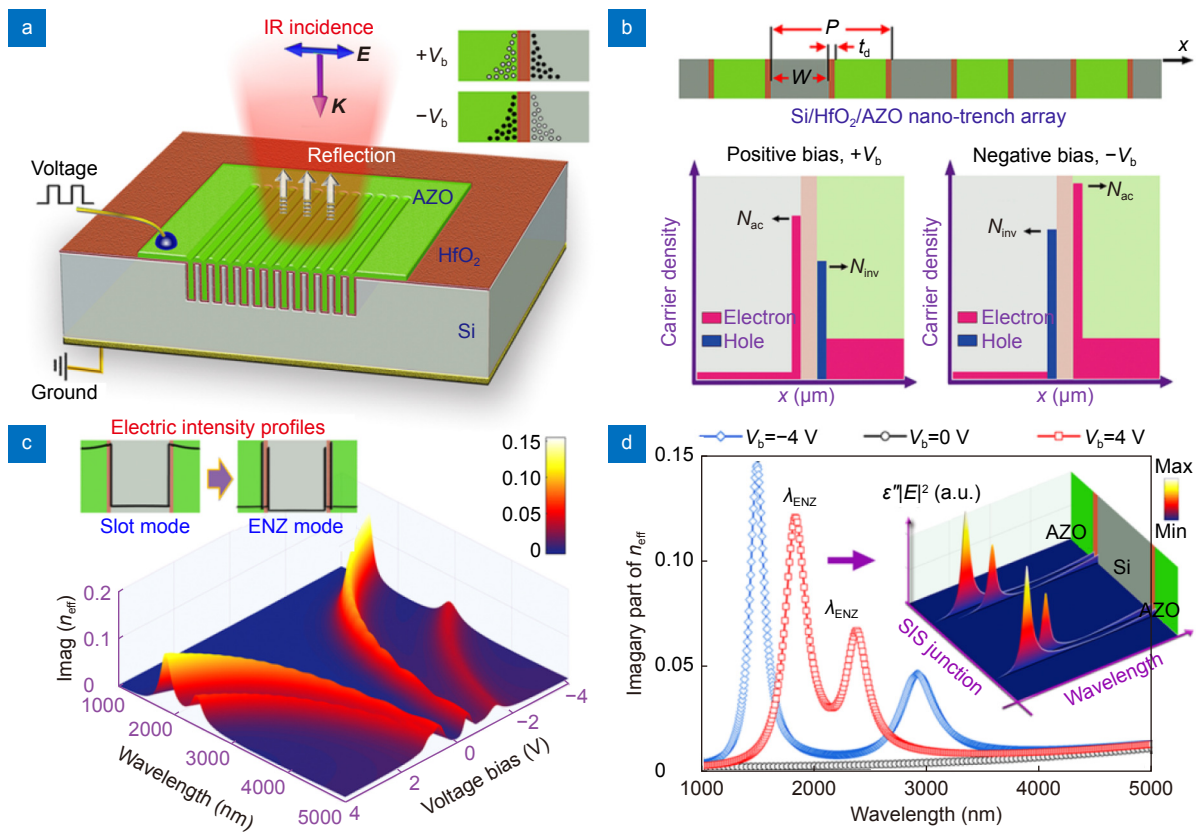As illustrated in Fig. 1(a), the proposed spatial light

Fig. 1 | (a–b) The schematic drawing of the deep nanotech-based SIS capacitor for broad-band spectral E-O modulation. Under external voltage biasing, the capacitor encounters charge accumulation at both sides of the SIS junction. With a sufficiently high carrier density, dual ENZ confinements can be anticipated in the nanometer thin layers which results in substantial E-O absorption along the sidewall of the nanotrench. Herein, the period of the nanotrench (P) is 300 nm, the width of the silicon wall is a half of the period ($W=P/2$), and the thickness of HfO$_2$ (t_d) is assumed to be 8 nm. The background doping level of AZO and silicon is 2×10^{18} and 2×10^{17} cm^{-3}, respectively. **(c)** The evolution of the mode loss characteristics in the SIS nanotrench as a function of wavelength and voltage bias. The upper plot shows two typical mode field profiles associated to with and without a voltage bias. **(d)** The imaginary part of the effective mode index (n_{eff}) plotted at three selected voltages (i.e., V_b=−4, 0 and 4 V). The inset is P_{abs} of the eigenmodes plotted in the spatial and spectral domains, which illustrates the localized energy absorption properties of the two distinct ENZ modes (V_b= 4 V).

modulation scheme is based on a semiconductor-insulator-semiconductor (SIS) nano-capacitor, in which a high aspect ratio Si nanotrench with an ultra-thin conformal coating of high k insulator (HfO$_2$) is assumed to be completely wrapped by Al-doped ZnO (AZO). Both the AZO and silicon are assumed to be n-type semiconductors which have moderate background doping level (N_0) to guarantee low optical loss in the IR regime. Imagining from a parallel plate capacitor (inset of Fig. 1(a)), equal and opposite surface charges (Q_s) induced by an external voltage bias (V_b) is given by $Q_s=C_s\times V_b$, where C_s is area capacitance. To outline the basic modulation principle of the proposed SIS nanotrench capacitor, we first consider a simplified electrical model[36,37] where the accumulation (inversion) layer of electrons (holes) within the semiconductors is in close proximity to the insulator with a constant thickness of t_s~1 nm (estimated by the

Thomas-Fermi screening length). The carrier distributions in the SIS capacitor with a sufficient voltage bias (assuming V_b=0 is the flat-band voltage), therefore, can be described as (Fig. 1(b)): $N_{ac}=Q_s/t_s+N_0$, the electron concentration of the accumulation layer for one side; $N_{inv}=Q_s/t_s-N_0$, the hole concentration of the inversion layer for the other side. In the IR regime, the complex permittivities of both silicon and AZO are concentration-dependent and can be well approximated by the free carrier model (i.e. Drude model) according to the early reports (see Supplementary information S1). With a sufficiently high carrier density, the crossover wavelength (i.e. ENZ point) of the surface carriers can be continuously modulated in a broad IR wavelength regime for the concentration levels related to the varying voltage bias (V_b) in the range of –4 to 4 V (Fig. S1).

Note that, the Si/HfO$_2$/AZO nanotrench array is

periodically arranged with a subwavelength pitch ($P \ll \lambda$) in the lateral direction while the depth keeps relatively long for the light propagation direction. Such a sub-wavelength nano-system allows for non-resonant and near perfect coupling with the free space incidence, and can be considered as a homogeneous medium with its optical properties described by the effective mode index according to the effective-medium theory (EMT)[46]. We therefore adopted the finite-difference eigenmode (FDE) solver to calculate the mode properties of the SIS nano-trench at different voltages (see Supplementary information S2 for more details). As shown in Fig. 1(c), for the case absent of any external voltage bias, the SIS capacitor in a flat-band condition exhibits a slot mode like feature of the electromagnetic field distribution which gives rise to lossless characteristic throughout a broad IR wavelength regime (1.5–5 μm). In contrast, when applying a voltage across the capacitor, high carrier density layers presented in both the AZO and silicon significantly alters the light propagation/absorption properties at the ENZ points as the IR light trends to couple with the ENZ modes. The resulting E-A efficiency represented by the imaginary part of mode effective index (k_{eff}) is illustrated in Fig. 1(c). There are two lossy bands with the peak positions coinciding with the ENZ points of AZO or silicon surface layers, which can be continuously tuned from NIR to MIR regions. Although the densities of surface carriers in the accumulation and inversion layers are close to each other at a given voltage bias, butthe high-frequency permittivity term in the Drude model for silicon is much larger than that for AZO (Supplementary information S1). This fact results in two distinct ENZ wavelengths for the biased capacitor where the silicon related ENZ mode always presents at the longer wavelength, as clearly verified by the spectral distribution of the normalized power density of the eigenmode absorption (inset of Fig. 1(d), defined as $P_{\mathrm{abs}} \propto \varepsilon'' |E|^2$). Considering a reflective-type device architecture (Figure 1(a)) where the IR light passing through the effective medium twice, the modulation depth can be approximated by the Beer's law: $M_{\mathrm{d}} = 1 - \mathrm{e}^{-2\alpha(\lambda)D}$, where α and D are the absorption coefficient ($4\pi k_{\mathrm{eff}}/\lambda$) and the thickness of the active medium (i.e., the depth of nanotrench). For a positive bias of 4 V, the dual ENZ modulation bands (λ=1830 and 2375 nm) shown in Fig. 1(d) can lead to a M_{d} up to 90% and 60% respectively with a nanotrench depth of 1.5 μm. The nanotrench system based spatial light modulation with an elongated LMI path allows a

larger absolute modulation depth as compared to previous plasmonic resonance-ENZ coupling strategies (typically the M_{d} is less than 20%)[41–43].

Experimental results of the broad-band E-O modulation

The experimental demonstration of above dual-ENZ modes mediated broadband modulation scheme was also carried out. The silicon nanotrench array with a pitch of 400 nm was defined via e-beam lithography and deep silicon etching process. The gate dielectric HfO_2 with a target thickness of 10 nm was prepared by atom layer deposition. To ensure the growth of AZO in a well encapsulated manner, pulse laser deposition (PLD) was used instead of the common sputtering method. The high temperature PLD facilitates the migration ability of adsorbed atoms on substrate and thus can offer high ability of lateral growth on the nanostructures with high aspect ratio, as confirmed in the Supplementary information S3. UV lithography combined with wet etching processes were carried out to leave a small rectangle area of AZO. Subsequently, the front anode electrode with an opening was defined on the AZO mesa. The opening is slightly larger than the area of nanotrench array (60×60 μm²), which allows us to evaluate the modulation property of the SIS capacitor for the reflection beam. Low resistive Ti/Au contact on the rear side of silicon substrate was considered as the ground. Fig. 2(a–b) shows the top-down and side-view SEM images of the fabricated capacitor. The thin layer of AZO can be clearly observed at the sidewalls of the nanotrenches in the Focus Ion Beam (FIB) sample (Fig. 2(b)). Note that, the relatively thick capping layer atop of the nanotrench also points to a preferential orientation growth tendency. This fact can be evidenced by the X-ray diffraction results (see Supplementary information S3), in which the strong (002) diffraction peak with a very narrow FWHM confirms a good quality and high c-axis orientated crystalline structure of the PLD prepared AZO.

The completed capacitors were mounted and wire-bonded to pads on a printed circuit board (Fig. 2(c), the upper plots). Focusing upon the dual-ENZ confinement mechanism, the E-O modulation property of the nanotrench SIS capacitor was examined in quasistatic measurements. The reflection spectrum was acquired using a microscope Fourier Transform Infrared Spectrometer (FTIR, Nicolet *i*N10), in which non-polarized beam can be tuned to match the active area of nanotrench capacitor.
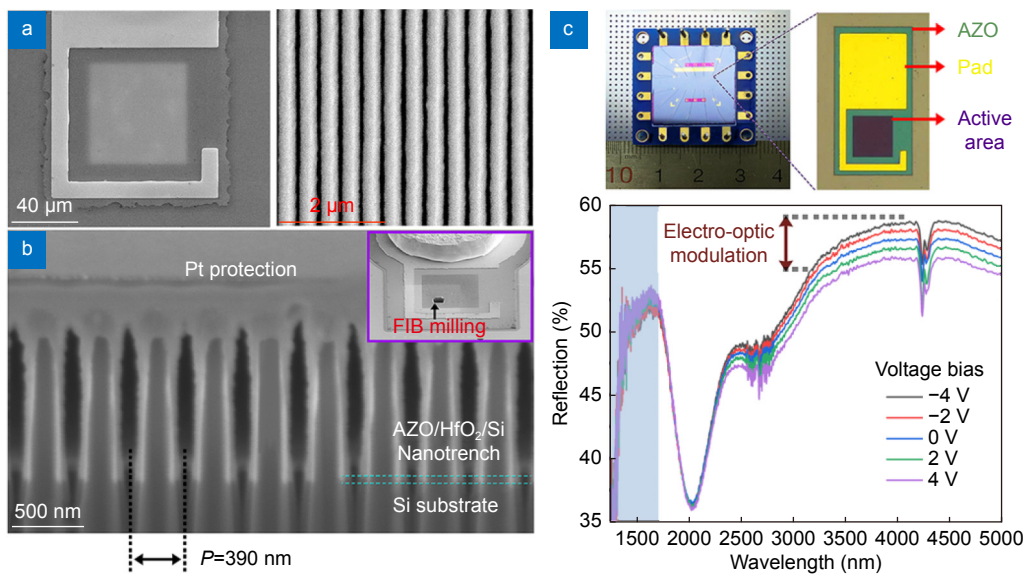
Fig. 2 | (a) Top view SEM images of the deepnanotrenchSIS capacitor. **(b)** Side view SEM image of the inner structure of the SIS nano-trenchesafter a section in the central region was milled by FIB.The etched nanowalls were slightly tapered, with the top and bottom widths ranging from 110 to 185 nm and the depthestimated to be 1.3 μm. **(c)** The photograph of fabricated device mounted on PCB (left) and the enlarged optical microscopy image of the device area. **(d)** The FTIR measured reflection spectra at various voltages.

Fig. 2(c) shows the measured reflection spectra at various biasing voltages. The reflection spectra was collected over a broad wavenumber range (8000 to 2000 cm^{-1}) but the short-wavelength part (marked as the shadow) of the spectrum becomes very noisy. For all the measured spectra, a shape and large reflection dip located at the wavelength of 2021 nm and a small dip at 2650 nm were observed. These features originate from the ENZ absorption or ray destructive interference, which will be validated later. At longer wavelengths, relative high reflection amplitudes were observed. By imposing different biasing voltages, repeatable variations of the reflection can be clearly observed in our measurements. As revealed in Fig. 2(c), the broadband E-O modulation behavior has been validated qualitatively regarding on the tunable reflection spectra over 2500 nm to 5000 nm. Nevertheless, we are aware of discrepancies when comparing with our previous theoretical results. Apparently, the demonstrated E-O modulation depth (M_d~3%) is much smaller than that of the theoretical expectations from Fig. 1(d). The M_d can be doubled by employing linear-polarized light modulation scheme, as the ENZ modes can only be excited by incidence that is tangentially polarized to the SIS interface plane. Another important discrepancy related to the experimental data is the monotonous increase of the E-A when tuning the bias from a negative gate voltage to a positive one, whereas the theoretical model suggests onset of the E-A at both positive and

negative biasing conditions (refer to Fig. 1(d)). This fact can be properly attributed to the large negative shifts of the electrical neutrality of the experimental devices.

To fully understand above experimental findings, more detailed optical and electrical investigations are needed. Fig. 3(a) shows the Infrared Spectroscopic Ellipsometry (IR-SE) data of the planar AZO/HfO$_2$/silicon structure prepared using the same procedure as the nanotrench capacitor. The measurement was conducted in the spectral range of 300–1680 nm at three angles of incidence (60°, 65°, and 70°). For the wavelengths larger than 1100 nm, the backside reflection passing through the transparent silicon substrate is incoherent with reflections from the top surface. This results in depolarization of the measurement beam as shown in the Fig. 3(a). Therefore, the optical model for the SE fitting should include the depolarization data. The optical constants the ITO layers were analyzed based on the Drude model. The fitting targets are the film thicknesses (roughness layer, AZO layer and HfO$_2$) and the Drude model's parameters (free carrier density, high frequency permittivity, and damping term). In Fig. 3(a), it is found that the measured depolarization, Psi and Delta data can be fitted very well with our optical model. The carrier concentration of AZO obtained herein is 3.3×10^{20} cm^{-3}. Based upon the derived Drude model's parameters, in Fig. 3(b), the complex permittivity of the as-prepared AZO can be extrapolated towards a wide spectrum. The ENZ
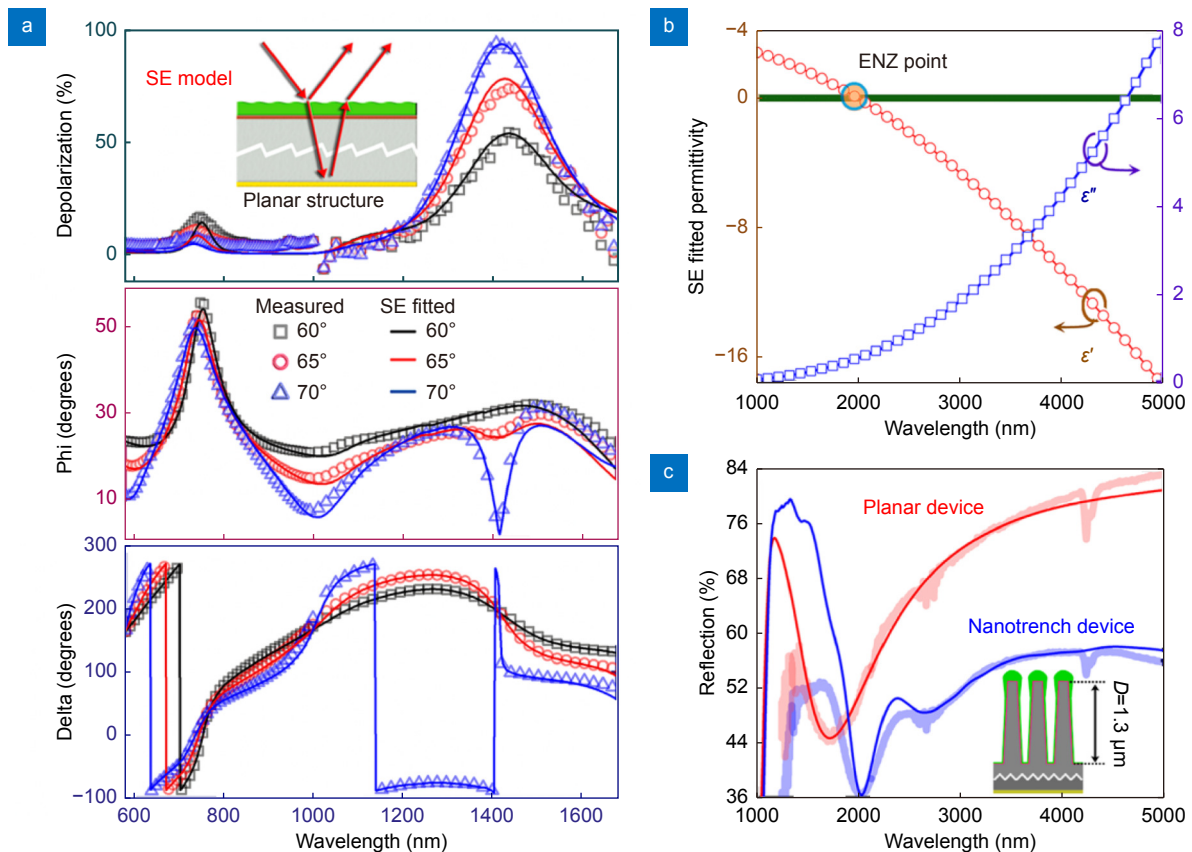
Fig. 3 | (**a**) The measured and fitted SE data of the planar reference structure with different incidence angles. The complete structure represented in SE model as a multilayered system (Inset of the top plot). (**b**) Optical constants of the PLD deposited AZO film based on the SE fitting. The derived values for the Drude model parameters are: high frequency permittivity ε_∞=3.806, carrier density N_0=3.3×10^{20} cm^{-3} and damping rate γ=1.39 ×10^{14} s^{-1}. Based on the SE model, the thickness of the AZO film and HfO$_2$ is found to be 343 and 10 nm, respectively. (**c**) Spectral fitting results of the nanostrench and the planar reference devices. The thick and thin curves represent the experimental and fitted results, respectively. Note that, the non-polarization response of nanotrench device is averaged by two orthogonal linear polarizations.

wavelength (λ_{ENZ}) represented by the crossover point of real part is found to be around 2000 nm and the corresponding imaginary part is smaller than one. Now, we can adopt the complex permittivity of AZO to mimic the optical property of the nanotrench and planar reference SIS capacitor *via* FDTD simulation. Most of the geometric parameters (e.g. nanotrench depth, width, thickness of HfO$_2$ and general morphology of AZO coating) used in the FDTD model can be directly measured from the SEM images (Fig. 2(a–b)) or roughly estimated from the beforehand calibrated fabrication process. Although the band bending effect may already exist in the static-state SIS capacitor, we neglect the surface carrier accumulation for the sake of simplicity. Therefore, both the AZO and silicon are assumed to be homogenous with intrinsic carrier related permittivity. As shown in Fig. 3(c), the main spectral features of the measured reflection for both the nanotrench and planar structure can be captured by our optical models (Supplementary information S4). In order to obtain a good match to the dominant reflection dip at 2020 nm, the background doping level of AZO in our nanotrench structure is calibrated to 3.1×10^{20} cm^{-3}. The slightly lowered carrier concentration can be attributed to the difference in the growth kinetics of the AZO deposited on the nanostructured and planar substrates. For the nanotrench case, the observed shape dip can now be safely ascribed to the ENZ absorption of the thin AZO shell. Regarding to the high background carrier level of AZO, the E-A response from the thin surface charge layer can differ significantly from the situations we consider in Fig. 1. In addition, there is an air gap between the fabricated nanotrenches. The continuity of the electric displacement at the interfaces gives the boundary conditions as: $\varepsilon_1 E_1$=$\varepsilon_2 E_2$. In the wavelengths of 3~5 μm, the unity permittivity of the air gap could be smaller than that of the ENZ layers (ε_{ENZ} equals the imaginary part of the materials' permittivity at the ENZ point). The electric field tends to be localized in

the air gap area rather than the ENZ layer. Therefore, the existence of the air gap in the fabricated structures could be an important issue leading to the unsatisfactory modulation performance.

We have previously posed a conjecture that unanticipated monotonous voltage-dependent E-O modulation property encountered in our experiments is related to the electrical neutrality shifts of the SIS capacitor. To demonstrate this, further studies concerning the realistic carrier tuning behavior under external voltage biasing should be carried out, for which we resort to the capacitance-voltage (C-V) measurements on the nano-capacitor and a planar reference (Fig. 4(a)). The two capacitors in comparison share similar C-V profiles at the given biasing voltages. Since the prepared AZO holds a sufficient high background carrier density which cannot be fully depleted at the given positive V_b, the observed high frequency C-V curves are very similar to a typical MOS capacitor. Upon a biasing voltage of V_b~4 V, consider-

ing the 3D wraparound junction of the nanotrench scenario, its capacitance per unit area is at least five-times larger than the planar capacitor. Small-signal AC device simulation with previous developed quantum model was also performed to fit the C-V profile of the planar capacitor (see Supplementary information S5 for more details). The trapped-state density on the order of 10^{12} cm^{-2} at the silicon/HfO$_2$ interface is found to be crucial for acquisition of the stretch-out property of the C-V curve. Moreover, regarding to the fact that the AZO has an electron affinity close to the silicon (4.05 eV), the large negative shifted C-V curve in measurement indicates the existence of the fixed charges at the interface. Thus, we have taken into account the above mentioned issues *via* implanting of the interface model (Supplementary information S6, Table 2). Fig. 4(a) shows that the experimental C-V profiles can be accurately fitted by the small-signal AC simulation. The derived carrier density of AZO is around 3.2×10^{20} cm^{-3}, which appears to be in
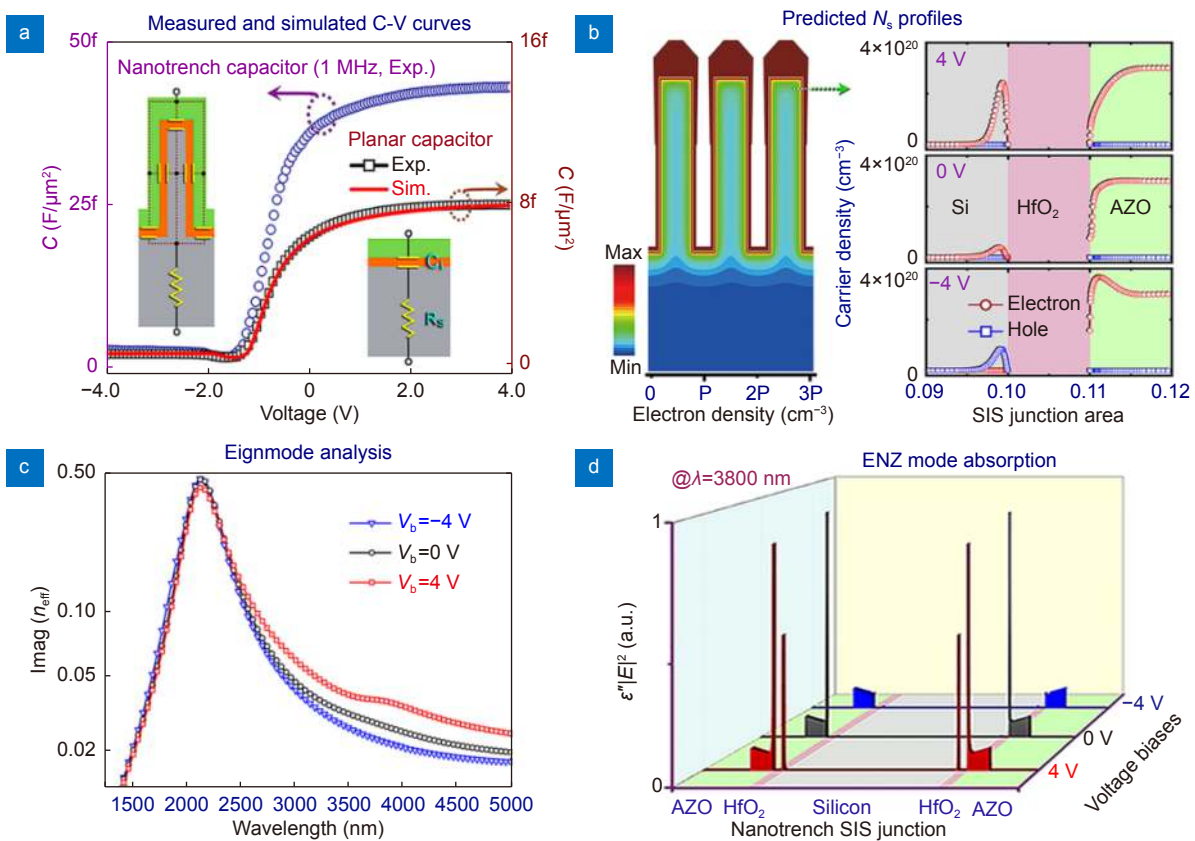

Fig. 4 | (**a**) The experimental measured high frequency C-V curves of the nanotrench and planar SIS capacitor (open symbols). The result of the planar reference was fitted very well with our electrical model (red line). (**b**) Voltage bias-dependent carrier profiles near the SIS junction area obtained from the TCAD modeling using the derived electrical parameters. (**c**) The imaginary part of the effective index of the fundamental mode supported by the SIS nanotrench. In the PDE calculations, the spatially varied optical constants of the SIS junction were extrapolated by the Drude model using the carrier profiles shown in (b). (**d**) The P_{abs} distribution across the SIS junction at a wavelength of 3800 nm representing the ENZ modes modulated by voltage biasing.

reasonably good accord with the SE fitted value. According to our simulation, a large negative V_{Fb} value of -1.27 V is determined, confirming the shifted electrical neutrality of the SIS capacitor.

The theoretical E-O modulation presented in Fig. 1 is based on the assumption that the local change of the surface carrier in semiconductors occurs in a constant thin layer. However, the actual profiles of the surface charge can differ significantly, which have to resort to the solution of the Poisson's equation for the SIS capacitor under electrostatic potential. Moreover, recent studies found that it is crucial to include the quantum effect beyond the classical device physics for fully understanding of the performance of ENZ modulation in practice[39,42]. To this end, to acquire more realistic carrier distributions, we perform the detailed device simulations of the SIS capacitor with the density gradient (D-G) quantum model (Supplementary information S6). Most electrical parameters used in our simulation are based upon the fitting results from the above SE and C-V studies. As shown in Fig. 4(b), with a negative bias of -4 V, the AZO side is in electron accumulation state while the silicon undergoes inversion that accompanied with a moderate high density of holes. For the zero bias case, surface depletion occurs in AZO and only a small amount of electron can be witnessed in silicon. At a positive bias of 4 V, the surface of AZO is forced into a deep depletion mode as inferred by the enlarged space-charge region. It is also notable that a high density of electron is accumulated at the surface of silicon. For revealing the corresponding E-A characters of the SIS capacitor, further optical mode analysis was performed by taking account of spatial carrier dispersion based on the above carrier profiles and the Drude model. Note that, the Drude model for AZO is modified according to the SE fitting results. The fundamental modes supported by the nanotrench capacitor under different voltages were calculated separately and the distribution of k_{eff} and P_{abs} are plotted in Fig. 4(c–d). The k_{eff} in a wavelength regime of 2500–5000 nm increases with the increasing voltage bias, which is closely consistent with our experimental observation (Fig. 2(c)). The corresponding E-A modulation can be qualitatively explained from the P_{abs} distributions along with the carrier profiles shown in Fig. 4(b). At a negative bias of -4 V, the surface accumulation layer in AZO has a peak electron density slightly higher than the background doping level. Its ENZ confinement effect might be almost submerged by the large background ENZ absorp-

tion related to the rest neutral region of AZO, resulting in a very limited increment of the mode loss at a short wavelength regime of 1500–2000 nm. Although the inversion hole was observed at the silicon surface, its carrier density is still not high enough for an ENZ permittivity in a mid-IR range (refer to P_{abs} plot). For the zero bias condition, the electron density of the surface depletion layer in AZO isgradually decreases into a lower carrier density towards the interface. This gives rise to an ENZ confinement at a mid-IR wavelength as confirmed by the P_{abs} plot (λ=3800 nm, V_b=0). Finally, for the case of positive voltage bias, both the surface electrons in the extended space-charge area of AZO and the accumulation layer of silicon hold a proper carrier profile to allow sufficient ENZ confinements. Dual ENZ confinements in the SIS capacitor can be clearly inferred from the P_{abs} plot (λ=3800 nm, V_b=4 V), which therefore results in the largest mode loss in the mid-IR range.

Transient analysis of the dual-ENZ E-O modulation

In practice, in addition to the modulation depth and operation wavelength range, another key performance indicator for an E-O modulator is the modulation speed. Although our proof-of-concept experiments were performed at a quasistatic state, its high frequency property can be partially inferred from the small signal C-V measurement. As illustrated in Fig. 4(a), the C-V curves measured at a megahertz frequency are highly asymmetric, suggesting that the fast E-O operation with negative switching voltage will be no longer functional because of the relatively slow carrier generation-recombination processes for the inversion state. Although the prototype design remains valid at positive bias conditions, the high background carrier concentration of AZO has been demonstrated to be unfavorable for mid-IR operation. Paradoxically, if we consider a lightly doped AZO for improving modulation depth, the carrier inversion rather than the partially depletion takes place in AZO for the forward-biased SIS capacitor, which again only allows for low frequency or quasistate E-O modulation. It becomes clear now that, for pursuing high speed and modulation depth, the doping polarity has to be different in the two semiconductors of SIS capacitor. Therefore, the optimum combination for the SIS capacitor is using p-type silicon along with n-type AZO. As shown in the energy band diagram of Fig. 5(a), when applying a negative voltage bias, both silicon and AZO undergo carrier

accumulation (hole and electron, respectively). Regarding on the ultra-fast majority carrier transport process, the switching speed of the capacitor is mainly determined by the RC delay time. To confirm this, transient device simulation (Supporting information S6) was carried out to investigate the carrier dynamics induced by the fast switching. The background doping levels in AZO and silicon are assumed to be 2×10^{18} and 6×10^{17} cm^{-3} respectively, which render the series resistance down to several Ohms and meanwhile low background optical absorption. No interface defect/trap model was included in these calculations as sophisticated surface passivation process can be properly adopted to reduce the surface defect density. The transient carrier response upon a step voltage signal (switch between 0 and −5.5 V) is shown in Fig. 5(b), which suggests that the rise and fall times of the device are 32 ns and 10 ns respectively.

Based on the Drude model, the calculated transient carrier profiles from electrical simulation were then incorporated to extrapolate the spatially varied material's permittivity in the nanotrench SIS junction. The whole capacitor structure in the scope of EMT can be de-

scribed as the simple multilayer system where the nanotrench layer is considered as a homogenous film with effective refraction index obtained from the 1D eigenmode calculation. Note that, to eliminate the unwanted intensive interference fringes in the calculated spectra, the thick substrate (e.g. 300 μm) was assumed to be a complete incoherent medium (for further details of the models, see Supplementary information S7). Based upon this semi-analytical approach, the changes of the reflectance of the capacitor at different time points can be obtained. The resulting transient and broad-band spectral modulation is given in Fig. 5(c). At the saturated state, the relative modulation depths are found to be 72% and 40% for the two dominate wavelengths associated with surface carrier induced ENZ confinements (i.e. 2030 nm and 3410 nm). Meanwhile, the proposed SIS device shows a switch speed less than 50 ns, thereby holding great promise for high speed spatial light modulation.

Conclusions

In summary, we proposed a broad-band spectral modulation scheme for spatial light by using electrically
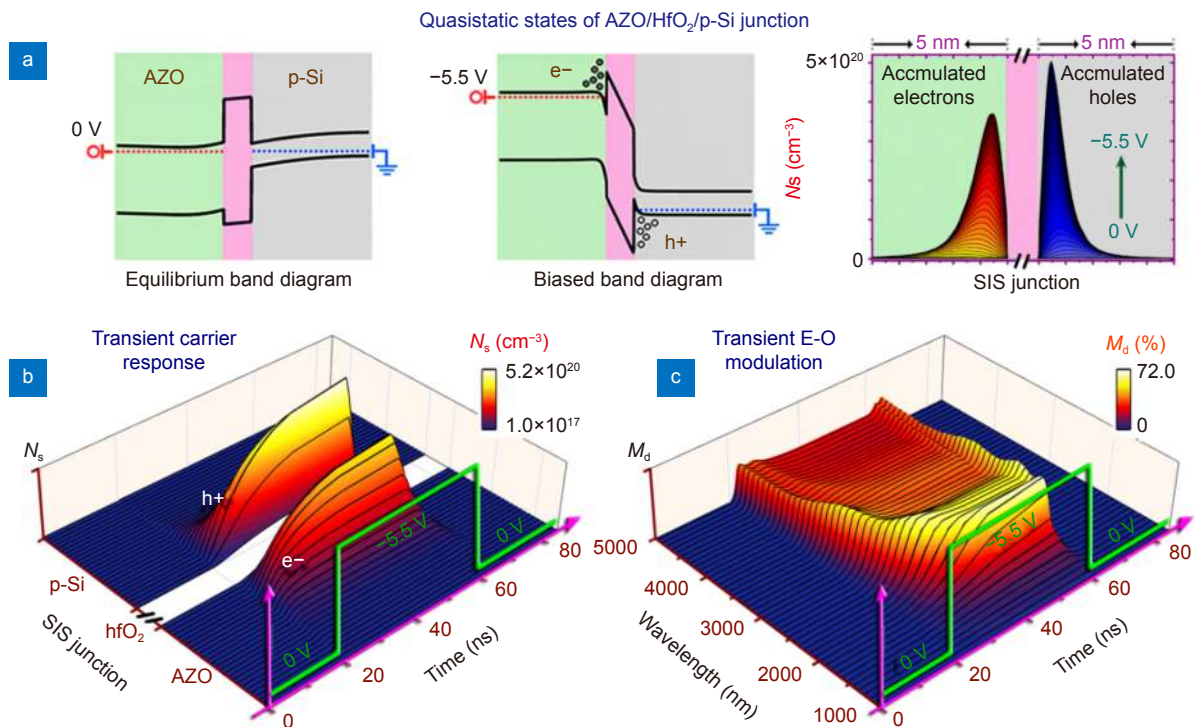

Fig. 5 | Transient E-O response of the AZO/HfO$_2$/p-Si capacitor to applied switching voltage. (a) Quasistatic-state band diagram of the SIS junction with and without an external voltage bias (left and middle plots). The evolution of carrier distribution near the SIS junction for the capacitor applied with gradually decreased voltages (right plot). **(b–c)** Transient carrier and E-O modulation of the proposed SIS capacitor. The E-O modulation property is calculated based on an optical model using the same geometry as that of Fig. 2 (i.e., AZO fully wrapped the nanotrench structure where the depth of the nanotrench is 1.5 μm. For the sake of reducing series resistance, the thickness of substrate is assumed to be 100 μm).

addressed dual ENZ confinements in a deep nanotrench-based SIS capacitor. While the free carrier electro-refraction effect in silicon is frequently used in E-O modulators, our results highlight the possibility to utilize electro-absorption effect in silicon through similar ENZ confinement scheme as the TCO materials. Based upon the TCO/HfO$_2$/silicon configuration, the field-effect induced surface charge layers adjacent to both sides of the SIS junction can lead to two lossy and well-confined ENZ modesthat contribute to substantial and broad-band light absorption along sidewalls of the deep trench. The broad-band E-O modulation characteristics of the SIS capacitor operated at steady-state were thoroughly analyzed and confirmed by theoretical and experimental studies. We demonstrated that the proposed E-O scheme with proper device optimization allows for high speed operation and large absolute modulation depth around 40–70% for a broad wavelength range between NIR and MIR. Utilizing the dual ENZ confinement effect in similar TCO/silicon-based SIS structures holds great potential to enable broad-band and high-speed spatial light modulation on the fully integrated silicon platform.

References

1. Efron U, Liverscu G. Multiple quantum well spatial light modulators. *Spatial Light Modulator Technology: Materials, Devices and Applications*, Efron U, Eds. ; Dekker: New York (1995).
2. Savage N. Digital spatial light modulators. *Nat Photonics* **3**, 170–172 (2009).
3. Maurer C, Jesacher A, Bernet S, Ritsch‐Marte M. What spatial light modulators can do for optical microscopy. *Laser Photonics Rev* **5**, 81–101 (2011).
4. Zhang YB, Liu H, Cheng H, Tian JG, Chen SQ. Multidimensional manipulation of wave fields based on artificial microstructures. *Opto-Electron Adv* **3**, 200002 (2020).
5. Chen Q, Nan XH, Chen MJ, Pan DH, Yang XG et al. Nanophotonic color routing. *Adv Mater* **33**, 2103815 (2021).
6. Wen L, Liang L, Yang XG, Liu Z, Li BJ et al. Multiband and ultrahigh figure-of-merit nanoplasmonic sensing with direct electrical readout in Au-Si nanojunctions. *ACS Nano* **13**, 6963–6972 (2019).
7. Chen Q, Liang L, Zheng QL, Zhang YX, Wen L. On-chip readout plasmonic mid-IR gas sensor. *Opto-Electron Adv* **3**, 190040 (2020).
8. Soref R, Bennett B. Electrooptical effects in silicon. *IEEE J Quant Electron* **23**, 123–129 (1987).
9. Alexander K, George JP, Verbist J, Neyts K, Kuyken B et al. Nanophotonic Pockels modulators on a silicon nitride platform. *Nat Commun* **9**, 3444 (2018).
10. Kuo YH, Lee YK, Ge YS, Ren S, Roth JE et al. Strong quantum-confined Stark effect in germanium quantum-well structures on silicon. *Nature* **437**, 1334–1336 (2005).
11. Asakawa K, Sugimoto Y, Nakamura S. Silicon photonics for telecom and data-com applications. *Opto-Electron Adv* **3**, 200011 (2020).
12. Reed GT, Mashanovich G, Gardes FY, Thomson DJ. Silicon optical modulators. *Nat Photonics* **4**, 518–526 (2010).
13. Reed GT, Mashanovich GZ, Gardes FY, Nedeljkovic M, Hu YF et al. Recent breakthroughs in carrier depletion based silicon optical modulators. *Nanophotonics* **3**, 229–245 (2014).
14. Wood MG, Burr JR, Reano RM. 7 nm/V DC tunability and milli-volt scale switching in silicon carrier injection degenerate band edge resonators. *Opt Express* **24**, 23481–23493 (2016).
15. Terada Y, Tatebe T, Hinakura Y, Baba T. Si photonic crystal slow-light modulators with periodic p–n junctions. *J Lightw Technol* **35**, 1684–1692 (2017).
16. Timurdogan E, Sorace-Agaskar CM, Sun J, Hosseini ES, Biberman A et al. An ultralow power athermal silicon modulator. *Nat Commun* **5**, 4008 (2014).
17. Haffner C, Heni W, Fedoryshyn Y, Niegemann J, Melikyan A et al. All-plasmonic Mach –Zehnder modulator enabling optical high-speed communication at the microscale. *Nat Photonics* **9**, 525–528 (2015).
18. Dionne JA, Diest K, Sweatlock KA, Atwater HA. PlasMOStor: a metal−oxide−Si field effect plasmonic modulator. *Nano Lett* **9**, 897–902 (2009).
19. Hassan SA, Lisicka-Skrzek E, Olivieri A, Tait RN, Berini P. Fabrication of a plasmonic modulator incorporating an overlaid grating coupler. *Nanotechnology* **25**, 495202 (2014).
20. Olivieri A, Chen CK, Hassan S, Lisicka-Skrzek E, Tait RN et al. Plasmonic nanostructured metal –oxide –semiconductor reflection modulators. *Nano Lett* **15**, 2304–2311 (2015).
21. Qiu CY, Chen CJ, Xia Y, Xu QF. Active dielectric antenna on chip for spatial light modulation. *Sci Rep* **2**, 855 (2012).
22. Shuai YC, Zhao DY, Liu YH, Stambaugh C, Lawall J et al. Coupled bilayer photonic crystal slab electro-optic spatial light modulators. *IEEE Photonics J* **9**, 7101411 (2017).
23. Zhou WD, Fan SH. Fano resonance photonic crystal filters and modulators. *Semiconduct Semimet* **100**, 149–188 (2019).
24. O'brien BB, Burns BE, Hu KL, Ionescu AC. Silicon spatial light modulator. *US Pat*, 5170283, 1992.
25. Lazarev G, Hermerschmidt A, Krüger S, Osten S. LCOS spatial light modulators: trends and applications. *Optical Imaging and Metrology* (Eds Osten W, Reingand N), John Wiley & Sons (2012).
26. Worchesky TL, Ritter KJ, Martin R, Lane B. Large arrays of spatial light modulators hybridized to silicon integrated circuits. *Appl Opt* **35**, 1180–1186 (1996).
27. Kulkarni OP, Islam MN, Terry FL. GaAs-based surface-normal optical modulator compared to Si and its wavelength response characterization using a supercontinuum laser. *Opt Express* **19**, 4076–4084 (2011).
28. Kuo YH, Lee YK, Ge YS, Ren S, Roth JE et al. Quantum-confined stark effect in Ge/SiGe quantum wells on Si for optical modulators. *IEEE J Sel Top Quant Electron* **12**, 1503–1513 (2006).
29. Audet RM, Edwards EH, Balram KC, Claussen SA, Schaevitz RK et al. Surface-Normal Ge/SiGe asymmetric Fabry–Perot optical modulators fabricated on silicon substrates. *J Lightw Technol* **31**, 3995–4003 (2013).
30. Yang YM, Lu J, Manjavacas A, Luk TS, Liu HZ et al. High-harmonic generation from an epsilon-near-zero material. *Nat Phys* **15**, 1022–1026 (2019).
31. Babicheva VE, Boltasseva A, Lavrinenko AV. Transparent con-

ducting oxides for electro-optical plasmonic modulators. *Nano-photonics* **4**, 165–185 (2015).

32. Hendrickson JR, Vangala S, Dass C, Gibson R, Goldsmith J et al. Coupling of epsilon-near-zero mode to gap Plasmon Mode for flat-top wideband perfect light absorption. *ACS Photonics* **5**, 776–781 (2018).

33. Gao Q, Li EW, Wang AX. Comparative analysis of transparent conductive oxide electro-absorption modulators [Invited]. *Opt Mater Express* **8**, 2850–2862 (2018).

34. Chen Q, Song SC, Wang HC, Liang L, Dong YJ et al. Ultra-broadband spatial light modulation with dual-resonance coupled epsilon-near-zero materials. *Nano Res* **14**, 2673–2680 (2021).

35. Nemati A, Wang Q, Ang NSS, Wang WD, Hong MH et al. Ultra-high extinction-ratio light modulation by electrically tunable metasurface using dual epsilon-near-zero resonances. *Opto-Electron Adv* **4**, 200088 (2021).

36. Krasavin AV, Zayats AV. Photonic signal processing on electronic scales: electro-optical field-effect nanoplasmonic modulator. *Phys Rev Lett* **109**, 053901 (2012).

37. Wood MG, Campione S, Parameswaran S, Luk TS, Wendt JR et al. Gigahertz speed operation of epsilon-near-zero silicon photonic modulators. *Optica* **5**, 233–236 (2018).

38. Amin R, Maiti R, Carfano C, Ma ZZ, Tahersima MH et al. 0.52 V mm ITO-based Mach-Zehnder modulator in silicon photonics. *APL Photonics* **3**, 126104 (2018).

39. Li EW, Gao Q, Chen RT, Wang AX. Ultracompact silicon-conductive oxide nanocavity modulator with 0.02 Lambda-Cubic active volume. *Nano Lett* **18**, 1075–1081 (2018).

40. Park J, Kang JH, Liu XG, Brongersma ML. Electrically tunable Epsilon-Near-Zero (ENZ) Metafilm absorbers. *Sci Rep* **5**, 15754 (2015).

41. Shi KF, Haque RR, Zhao BY, Zhao RC, Lu ZL. Broadband electro-optical modulator based on transparent conducting oxide. *Opt Lett* **39**, 4978–4981 (2014).

42. Liu XG, Kang JH, Yuan HT, Park J, Kim SJ et al. Electrical tuning of a quantum plasmonic resonance. *Nat Nanotechnol* **12**, 866–870 (2017).

43. Liu XG, Kang JH, Yuan HT, Park J, Cui Y et al. Tuning of Plasmons in transparent conductive oxides by carrier accumulation. *ACS Photonics* **5**, 1493–1498 (2018).

44. Hu X, Chen Q, Wen L, Jin L, Wang HC et al. Modulating spatial light by grating slot waveguides with transparent conducting oxides. *IEEE Photonic Technol Lett* **28**, 1665–1668 (2016).

45. Howes A, Wang WY, Kravchenko I, Valentine J. Dynamic transmission control based on all-dielectric Huygens metasurfaces. *Optica* **5**, 787–792 (2018).

46. Lalanne P, Lemercier-Lalanne D. Depth dependence of the effective properties of subwavelength gratings. *J Opt Soc Am A* **14**, 450–459 (1997).

Acknowledgements

Competing interests

The authors declare no competing financial interests.

Supplementary information

Supplementary information for this paper is available at
https://doi.org/10.29026/oea.2022.200093